Received: 6 November 2021 | Revised: 20 May 2022 | Accepted: 23 May 2022

DOI: 10.1002/cne.25378

RESEARCH ARTICLE

JCN RESEARCH IN SYSTEMS NEUROSCIENCE THE JOURNAL OF COMPARATIVE NEUROLOGY WILEY

Local targets of T-stellate cells in the ventral cochlear nucleus

Lin Lin Ph.D | **Jay Campbell Mr.** | **Donata Oertel Ph.D**[†] | **Philip H. Smith Ph.D**

Department of Neuroscience, University of Wisconsin-Madison School of Medicine and Public Health, Madison, Wisconsin, USA

Correspondence
Philip H. Smith, Department of Neuroscience, University of Wisconsin-Madison School of Medicine and Public Health, WIMR Room 3451, 1111 Highland Avenue, Madison, WI 53705-2275, USA.
Email: phsmith@wisc.edu

[†]Deceased: Dr. Oertel passed away April 22, 2020

Funding information
NIH, Grant/Award Numbers: R01DC016861

Abstract

T-stellate cells in the ventral cochlear nucleus (VCN) are known to have local axon collaterals that terminate in the vicinity of their dendrites and cell bodies within the same isofrequency lamina in parallel with the auditory nerve fibers that innervate them. Excitatory synaptic connections between stellate cells within an isofrequency lamina are hypothesized to be involved in the nitric oxide-mediated upregulation of T-stellate responses to their auditory input. This could serve as a mechanism of variable gain control in the enhancement of responses to vowel spectral peaks. Previous studies have provided indirect evidence for these possible synaptic interconnections between T-stellate cells, but unequivocal identification has yet to be established. Here, we used retrograde neuronal tracing with adeno-associated viral vector or biotinylated dextran amine injected into the inferior colliculus (IC) to detect the postsynaptic target of T-stellate cells within the VCN. We show that backfilled T-stellate cell axons make monosynapatic connections on the labeled cell bodies and dendrites of other labeled T-stellate cells within an isofrequency lamina. Electron microscopy revealed that T-stellate terminals can also make synapses on structures not retrogradely labeled from the IC. Glycine antibodies combined with the viral labeling indicated that these nonbackfilled structures that the labeled T-stellate terminals were synapsing on are most likely the cell bodies and dendrites of two size categories of glycinergic VCN cells, whose sizes and relative numbers indicated they are the D- and L-stellate cells. These cells are known to provide inhibitory inputs back onto T-stellate cells. Our data indicate that, in addition to their auditory nerve input, T-stellate cells provide a second modulatable excitatory input to both inhibitory and excitatory cells in a VCN isofrequency lamina and may play a significant role in acoustic information processing.

KEYWORDS
circuity, monosynapatic connection, T-stellate cell, ventral cochlear nucleus

1 | INTRODUCTION

As the first stage in the central auditory pathway, the cochlear nucleus (CN) integrates and processes acoustic information coming from the cochlea via separate, well-defined populations of neurons. These populations give rise to widespread projections throughout the brainstem and thalamus via multiple, parallel pathways. One of these pathways arises from glutamatergic T-stellate cells in the ventral CN (VCN). Individual T-stellate cells convey information about the envelope of an amplitude-modulated sound (Laudanski et al., 2010; Rhode & Greenberg, 1994) with the carrier frequency at or near the characteristic frequency of the cell. As a population, T-stellate cells provide a superior representation of vowel formant structure over a wide range of stimulus intensities in quiet or in background noise (Blackburn & Sachs, 1990; May et al., 1998). Such acoustic information is critical for understanding speech (Blackburn & Sachs, 1990; Shannon et al., 1995).

T-stellate cells are the predominant excitatory cell type in the multipolar cell region of the posterior VCN (pVCN) and are also intermingled with other cell types in the nerve root area separating the pVCN from the anterior VCN (aVCN), as well as in the aVCN (Brawer et al., 1974; Doucet & Ryugo, 1997; Oertel et al., 1990; Osen, 1969). The multiple highly branched dendrites of T-stellate cells commonly run parallel to the path of tonotopically arranged auditory nerve fibers (ANFs) from which they receive acoustic inputs (Doucet & Ryugo, 1997; Ferragamo et al., 1998; Oertel et al., 1990). T-stellate cells also receive glycinergic inhibitory inputs from three CN cell types, tuberculoventral cells in the dorsal cochlear nucleus (Campagnola & Manis, 2014; Wickesberg & Oertel, 1988; Wickesberg et al., 1991; Xie & Manis, 2013), D-stellate cells (Doucet & Ryugo, 1997; Oertel, 1984; Oertel et al., 1990; Oertel et al., 2011; Sento & Ryugo, 1989; Xie & Manis, 2014) that sparsely populate the VCN, and the more numerous L-stellate cells (Ngodup et al., 2020) in the VCN.

The axons of T-stellate cells project out of the CN via the ventral acoustic stria and give off collateral branches to multiple auditory brainstem nuclei before terminating in the contralateral central nucleus of the inferior colliculus (IC; Schofield & Cant, 1996). In the ICC, the terminals of T-stellate cells, as well as terminals from some cells in the ipsilateral intermediate nucleus of the lateral lemniscus, medial superior olive, and contralateral lateral superior olive, may be identified by their expression of both vesicular glutamate transporter 1 and 2 (VGLUT1 and VGLUT2; Ito & Oliver, 2010). Neural nitric oxide synthase (nNOS) is postsynaptic to the terminals thought to arise from T-stellates (Olthof et al., 2019) in a complex with glutamate N-methyl-D-aspartate (NMDA) receptors, soluble guanylyl cyclase (sGC, the nitric oxide [NO] receptor) and PSD95 (the postsynaptic density protein that anchors receptors and enzymes at the postsynaptic density). Activation of these NMDA receptors enhanced sound-driven activity in the ICC mediated by nNOS and sGC activation, indicating a role for NO in modulating ICC cell responses to incoming auditory stimuli (Olthof et al., 2019). Within the CN, the axons of T-stellate cells also give rise to local collaterals in the VCN, whose terminals remain in or close to the isofrequency lamina of the cell (Ferragamo et al., 1998; Oertel et al., 1990, 2011; Wu & Oertel, 1984). It has been assumed but not verified that these terminals of T-stellate cells synapse on other T-stellate cells and, together with auditory nerve (AN) terminals, provide glutamatergic input (Oertel et al., 2011). However, dual recordings from T-stellate cells separated by 180–230 μm but within the same isofrequency lamina in brain slices revealed that excitatory interconnections were rare and, if present, were likely polysynaptic based on latency (Oertel et al., 2011). As seen in the ICC, NO synthesis and release in the CN caused by T-stellate depolarization and NMDA receptor activation could potentiate the response to incoming auditory stimuli (Cao, Lin, Sugden, et al., 2019). Again, as in the ICC, this implicates NO activation as a means of upregulating responses to auditory stimuli. Such interconnections between T-stellate cells could serve as a central gain control in normal hearing and potentially generate hyperexcitability and perhaps induce tinnitus in the face of hearing loss.

To test whether T-stellate cells have monosynaptic connections with other T- stellate cells and could thus act as the connecting interneuron, we used neuronal tracing in transgenic and wild-type mice, confocal microscopy, electron microscopy, and immunohistochemistry to investigate and identify the local targets of axon collaterals of T-stellate cells within the VCN. We found that T-stellate cells directly synapse on both the soma and dendrites of other T-stellate cells, verifying monosynaptic connections between T-stellate cells. Multiple presynaptic T-stellate boutons could be observed on the same postsynaptic T-stellate cells, indicating a positive feedback network formed by interconnected T-stellate cells.

We also demonstrate that T-stellate cells can make monosynaptic contacts with glycinergic inhibitory neurons in the VCN. Measurements of the soma sizes of these glycinergic cells receiving T-stellate inputs indicate two populations likely representing the D- and L-stellate cells. Monosynaptic excitatory inputs from T-stellate cells onto glycinergic neurons may contribute to their tuning properties as well as their ability to detect narrowband signals masked by broadband noise (Gai & Carney, 2008; Palmer et al., 1996). In addition, we have previously shown that D-stellate cells are capable of releasing NO that can amplify the effects of their T-stellate excitatory inputs (Cao et al., 2019). Thus, T-stellate terminals could also potentially regulate the activity of both excitatory and inhibitory cells that are vital components of the VCN circuitry.

2 | MATERIALS AND METHODS

2.1 | Animals

Experiments were conducted in accordance with the Guide for the Care and Use of Laboratory Animals of the National Institute of Health, and protocols were approved by the Animal Care and Use Committee of the University of Wisconsin-Madison (UW-Madison) School of Medicine and Public Health.

Eight loxP-STOP-loxP-tdTomato Cre reporter mice (Ai14, Jackson Laboratory (Bar Harbor, ME) 007914; Madisen et al., 2010) of either sex were used in the adeno-associated viral (AAV) tracing experiments,

and four CBA/CaJ mice (Jackson Laboratory 000654) of either sex were used in the 3,3′-diaminobenzidine (DAB) tracing experiments. Animals from both strains ranged in age from 9 to 14 weeks old and weighed 23–29 g. Animals had unlimited access to food and water and were housed in a 12 h light/dark cycle.

2.2 | Stereotactic surgeries and injections

To label T-stellate cells in the VCN, stereotactic surgeries to introduce viral vectors or biotinylated dextran amine (BDA) into the contralateral IC were performed. Mice were anesthetized with isoflurane (~3%) in 100% oxygen and then placed in the stereotaxic apparatus. The anesthesia was maintained at 1–2% in 100% oxygen. Meloxicam (2–4 mg/kg) was administered subcutaneously as preemptive analgesia. An incision was made to reveal the skull, and a small hole (2 mm) was drilled above the IC. The stereotactic coordinates used to locate IC were 5.7 mm (for Ai14 mice) or 5.4 mm (for CBA/CaJ mice) posterior to Bregma, 1.3 mm lateral to Bregma, and 1.3 mm from the surface of the brain. A total of 60–80 nl of AAV vector (rAAV2-retro-pkg-Cre, Addgene (Watertown, MA) 24593-AAVrg; Tervo et al., 2016) or 400 nl of BDA (3000 MW, Invitrogen, 10% in sodium citrate-HCl, pH = 3) was loaded into a glass pipette with a tip diameter of 10–15 μm, and pressure was injected into the IC at a rate of 1 nl/s. The pipette was left in place for 5–10 min following the injection before it was slowly removed. The hole in the skull was left open and typically healed within 14 days. The incision was sutured, and the animal was returned to the home cage and allowed to recover.

2.3 | Immunohistochemistry

Fourteen to 23 days following the injection of the AAV vector into the IC, mice were anesthetized with ketamine (100 mg/kg)/xylazine (10 mg/kg) and transcardially perfused with 0.01 M phosphate-buffered saline (PBS, 137 mM NaCl, 2.7 mM KCl, 8 mM Na_2HPO_4, and 2 mM KH_2PO_4) containing 10 IU/ml heparin followed by 4% paraformaldehyde (PFA) in 0.01 M PBS. The brains were then removed and postfixed in the same fixative overnight at 4°C. After being rinsed three times in PBS, the brains were cut into 40–60 μm thick coronal or sagittal sections with a vibratome (VT-1000S, Leica, Wetzlar, Germany).

Sections were placed in 24-well plates and processed with gentle agitation. All immunohistochemistry steps were performed on free-floating sections, and all reagents were made up in 1x0.01 M PBS with 0.05% Tween (PBST) unless otherwise specified. After being permeabilized with 0.3% TritonX-100 in PBS for 20 min, sections were blocked with a blocking solution consisting of 5% normal donkey serum (NDS), 1.5% bovine serum albumin (BSA), and 0.3% TritonX-100 for 1 h. The blocking solution was then replaced with primary antibodies diluted in 1% BSA and 0.3% TritonX-100 overnight at room temperature. The primary antibodies used were guinea pig anti-VGLUT2 (MilliporeSigma (Burlington, MA) Cat # AB2251-I, RRID: AB_2665454, used at 1:500) or chicken anti-VGLUT2 (Synaptic Systems [Gottingen, Germany] Cat # 135 416, RRID: AB_2619824, used at 1:1000) and rabbit anti-PSD95 (Thermo Fisher Scientific [Waltham, MA] Cat # 51–6900, RRID: AB_2533914, used at 1:300). For a subgroup of sections, guinea pig anti-VGLUT1 (MilliporeSigma Cat # AB5905, RRID: AB_2301751, used at 1:1000) was also added. Sections were then rinsed and stained with corresponding secondary antibodies (listed in Table 2) for 2 h at room temperature. After counterstaining with 4′,6-diamidino-2-phenylindole (DAPI, Cat # D9542, Sigma–Aldrich, St. Louis, MO), sections were mounted on glass slides in VECTASHIELD® Antifade Mounting Medium (Cat # H-1000, Vector Laboratories, Newark, CA), coverslipped and sealed.

To visualize glycinergic neurons, a subset of AAV-injected animals (n = 3) were transcardially perfused with 0.01 M PBS containing 10 IU/ml heparin followed by a mixture of PFA and glutaraldehyde (0.2–1.5%) summed to 4%. The brains were removed and postfixed in the same fixative overnight at 4°C. The brains were then rinsed in PBS and cryoprotected in 30% (w/v) sucrose for frozen sectioning. Frozen sectioning was performed by the Translational Research Initiatives in Pathology Laboratory at UW-Madison. Every other or every third 10–12 μm thick coronal section was collected for later immunohistochemical processing.

Glass slides with premounted sections were rinsed with 0.1 M phosphate buffer (PB, pH = 7.4) and incubated in excess 1% sodium borohydride in PB (freshly prepared) for 25 min to reduce background glutaraldehyde fluorescence. After extensive rinsing, circles were drawn around the sections with a PAP pen. These sections were permeabilized and blocked as above and then incubated with the following primary antibodies (listed in Table 1) diluted in 1% normal donkey serum (NDS) and 0.3% TritonX-100 overnight at 4°C: guinea pig anti-VGLUT2 (1:500), chicken anti-VGLUT2 (1:500), rabbit anti-glycine (MilliporeSigma, Cat # AB139, RRID: AB_90582, used at 1:500) and mouse anti-tubulin βIII (TUBB3, BioLegend [San Diego, CA] Cat # 801201, RRID: AB_2313773, used at 1:500-800). After rinsing, sections were incubated with corresponding secondary antibodies (listed in Table 2) diluted in the same solution for 1 h at room temperature. The PAP pen circles were removed, and sections were mounted, coverslipped, and sealed.

Images of the IC and the CN were acquired with a confocal microscope (Nikon A1RS) using 10x (0.3 NA), 20x (0.74 NA), or 100x (1.4 NA) objectives, and tiled images were automatically stitched with NIS-Elements software (Nikon) during image acquisition.

2.4 | Antibody characterization

The VGLUT2 antiserum (MilliporeSigma Cat # AB2251-I, RRID: AB_2665454) was made against the C-terminal sequence of rat VGLUT2. Immunostaining using this antibody detects VGLUT2 in the thalamus of mice but not in the VGLUT2-negative central amygdala (Zhang et al., 2020). Another VGLUT2 antibody (Synaptic Systems Cat # 135 416, RRID: AB_2619824) recognizes a synthetic peptide corresponding to amino acids 566 to 582 from rat VGLUT2 and was

TABLE 1 Primary antibodies used in the study

Antibody	Immunogen	Source	Dilution
Anti-vesicular glutamate transporter 2 (VGLUT2)	KLH-conjugated linear peptide corresponding to the C-terminal sequence of rat VGluT2	Guinea Pig polyclonal, MilliporeSigma Cat# AB2251-I, RRID: AB_2665454	1:500
Anti-VGLUT2	Synthetic peptide corresponding to AA 566 to 582 from rat VGluT2	Chicken polyclonal,Synaptic Systems Cat# 135 416, RRID: AB_2619824	1:1000
Anti- VGLUT1	Synthetic peptide from rat VGLUT1 protein with no overlap to VGLUT2	Guinea Pig polyclonal, MilliporeSigma Cat# AB5905, RRID: AB_2301751	1:1000
Anti-glycine	Glycine-gluteraldehyde-bovine serum albumin	Rabbit antiserum, MilliporeSigma Cat# AB139, RRID: AB_90582	1:500/1000
Anti-postsynaptic density protein 95 (PSD-95)	KLH-conjugated synthethic peptide derived from the C-terminal region of human PSD-95	Rabbit polyclonal,Thermo Fisher Scientific Cat# 51-6900, RRID: AB_2533914	1:300
Anti-tubulin βIII antibody	The last 15 C-terminal residues of neuron specific Class III β-tubulin derived from rat brain	Mouse monoclonal, BioLegend Cat# 801201, RRID: AB_2313773	1:500

TABLE 2 Secondary antibodies used in the study

Secondary antibody	Conjugated	Source	Dilution
Anti-rabbit IgG (H + L) highly cross-adsorbed	Alexa Fluor 488	Donkey, polyclonal, Thermo Fisher Scientific Cat# A-21206, RRID: AB_2665454	1:500
Anti-guinea pig IgG (H + L) highly cross-adsorbed	CF 633	Donkey, polyclonal, Sigma–Aldrich Cat# SAB4600129, IRRID: AB_2890636	1:500
Anti-rabbit IgG (H + L)	DyLight 405	Donkey, polyclonal, Jackson ImmunoResearch Labs Cat# 711-475-152, RRID: AB_2340616	1:200
Anti-chicken IgY (IgG; H + L)	Alexa Fluor 647	Donkey, polyclonal, Jackson ImmunoResearch Labs Cat# 703-605-155, RRID: AB_2340379	1:500
Anti-guinea pig IgG (H + L) highly cross-adsorbed	CF 488A	Donkey, polyclonal, Sigma–Aldrich Cat# SAB4600033, RRID: AB_2890881	1:500
Anti-rabbit IgG (H + L) preadsorbed	Alexa Fluor 647	Donkey, polyclonal, Abcam Cat# ab150063, RRID: AB_2687541	1:500
Anti-mouse IgG (H + L)	DyLight 405	Donkey, polyclonal, Jackson ImmunoResearch Labs Cat# 715-475-150, RRID: AB_2340839	1:125

reported to detect a single band of appropriate molecular weight on western blots (manufacturer's specification). Immunostaining with these two VGLUT2 antibodies showed the same pattern of labeling in the CN in our experiments. The VGLUT1 antiserum (MilliporeSigma Cat # AB5905, RRID: AB_2301751) was made against the C-terminal sequence of rat VGLUT1. Immunostaining using this antibody detects VGLUT1 in wild-type mouse tissue but not in knockout mice (Murao et al., 2017). The PSD95 antibody (Thermo Fisher Scientific Cat # 51–6900, RRID: AB_2533914) was made against a synthetic peptide derived from the C-terminal region of human PSD95. It has been widely used for immunostaining and western blotting of mice. The glycine antiserum (MilliporeSigma Cat # AB139, RRID: AB_90582), made against glycine-gluteraldehyde-BSA, has minimal cross-reactivity with other conjugated amino acids or unconjugated glycine on ELISA or RIA (manufacturer's specification). The specificity of this antibody has been described by Kalloniatis & Fletcher (1993) and by Bäurle et al. (1997). The TUBB3 antibody (BioLegend Cat # 801201, RRID: AB_2313773) is a monoclonal antibody recognizing an epitope located within the last 15 C-terminal residues of neuron-specific Class III β-tubulin. This antibody detects bands of appropriate molecular weight on Western blots (Lee et al., 1990) and has been widely used as a neuronal marker.

2.5 | Electron microscopy

Five to 10 days after the stereotactic injection of BDA, mice were anesthetized with ketamine (100 mg/kg)/xylazine (10 mg/kg) and transcardially perfused with 0.1 M PB followed by a mixture of 2% PFA and

2.5% glutaraldehyde in 0.1 M PB. The brains were then removed and postfixed in the same fixative for at least 4 days at 4°C. Then, the brains were embedded in blocks of gelatin-albumin and cut into 70-μm coronal sections with a vibratome. All sections through the CN and IC were kept in series order and incubated overnight with avidin-biotin complex solution (VECTASTAIN® Elite ABC-HRP Kit, Peroxidase, Cat # PK-6100, Vector Laboratories). After washes with PB, sections were incubated with nickel/diaminobenzadine (DAB) solution containing 0.005% DAB tetrahydrochloride hydrate, 0.02% nickel ammonium sulfate, and 0.025% cobalt chloride in PB buffer for 20 min. Subsequently, hydrogen peroxide was added to yield a final concentration of 0.032%, and sections were incubated for an additional 15 min and then rinsed with PB.

Selected sections through the VCN containing darkly labeled cells were postfixed with 1% osmium tetroxide for 15 min, dehydrated in ascending grades of alcohol and epoxy-propylene oxide and then flat-embedded in EMBed-812 resin (Cat # 14900, Electron Microscopy Science, Hatfield, PA) between two sheets of Aclar film. The samples were then cured in an oven at 65°C overnight and viewed with a light microscope. Those containing numerous labeled cells were trimmed and resectioned into semithin (3 μm) sections. Selected 3 μm sections were remounted and ultrathin (70 nm) sectioned with an ultramicrotome (Leica EM UC6). The ultrathin sections were collected on grids with formvar support film and stained in 2.5% uranyl acetate (in 50% EtOH) for 10 min and then in Reynold's lead citrate solution for another 10 min. Images were acquired with a Tecnai 12 transmission electron microscope with an AMT BioSpirit12 camera and processed with Adobe Photoshop (Adobe Inc., San Jose, CA) and Fiji software (ImageJ).

2.6 | Image analysis

Image analyses were performed using Fiji software (ImageJ, NIH). To measure the size of T-stellate cells, the cell bodies of BDA-labeled neurons in the pVCN, aVCN, and nerve root areas from two mice were examined under a light microscope with a 60X objective, and their outlines were drawn using a camera lucida. These were digitally captured, and the diameter and silhouette somatic area of cell bodies were measured. For glycinergic neurons, confocal image stacks containing these neurons were projected, and the somatic area, longest diameters, and shortest diameters were measured. Each synaptic punctum was also measured and classified according to the target site (cell bodies, proximal dendrites attached to cell bodies, severed dendrites). The diameters of the contacted dendrites were measured at the targeted site. Reconstruction of the representative cell bodies and dendrites of T-stellate cells connected by boutons was rendered with IMARIS software (Oxford Instruments, Abingdon, UK) using the surface function.

For EM, images were stitched using Adobe Photoshop (Adobe Inc., San Jose, CA) and adjusted to optimize brightness and contrast when necessary. To compare with previous reports of the extent of synaptic coverage (Smith & Rhode, 1989), the circumferences of BDA-labeled T-stellate cells containing their nuclei were drawn, and circumference length was measured using Fiji software (ImageJ). The length of apposition of each synaptic terminal on a T-stellate profile was measured, and the percent of coverage (combined terminal apposition/T-stellate profile circumference) was calculated.

2.7 | Statistical analysis

All statistical analyses were performed in Origin (OriginLab Corporation, Northampton, MA), except for the dip test, which is performed in R 4.0.5 (R Core Team, 2021) with the diptest package (v0.75-7). Data values are reported as the mean ± *SD* unless stated otherwise. The number of objectives assessed and the number of animals from which they were imaged are indicated in the text. The results were considered statistically significant at $p < .05$. Plots were generated using Origin.

3 | RESULTS

3.1 | Identification of T-stellate cells in the VCN

T-stellate cells, also referred to as planar multipolar cells (Doucet & Ryugo, 1997), dominate the multipolar cell area of the pVCN between the nerve root and the octopus cell area. Some are additionally located in the nerve root as well as the aVCN anterior to the nerve root, where they intermingle with globular and spherical bushy cells (Brawer et al., 1974; Cant, 1981; Osen, 1969). T-stellate cells are the only known VCN principal neurons that project to the contralateral IC (Adams, 1979, 1983; Cant, 1982; Darrow et al., 2012; Oliver, 1987; Ryugo et al., 1981). We injected the rAAV2-retro-Cre vector into the ICC of *Ai14* mice (Figure 1a) to enable the expression of tdTomato in all cells projecting into this area, including T-stellate cells in the VCN. The localized stereotaxic administration of a small volume of vector consistently resulted in restricted injection sites in the IC on one side ($n = 5$, Figure 1b). Coronal ($n = 3$) and sagittal ($n = 2$) sections of the brainstem containing the contralateral CN were cut with a vibratome. In the coronal planes, labeled T-stellate cells that expressed tdTomato (subsequently referred to as tdTomato labeled T-stellate cells for simplicity) and their processes are confined to a medial-to-lateral band (dashed lined, Figure 1c) across the posterior to anterior extent of the nucleus. The band may contain a single or a few parallel isofrequency laminae. A bundle of labeled axons of T-stellates was observed leaving the VCN via the ventral acoustic stria (asterisks, Figure 1c). In the sagittal planes, labeled T-stellate cells clustered in two bands parallel to the direction of the ANFs in the pVCN and aVCN (data not shown). The width of the bands varied between animals. tdTomato-labeled neurons were rarely found in the ipsilateral VCN (four or fewer neurons per section, $n = 6$ sections from three animals).

Using BDA-labeled T-stellate cells, we compared their sizes between different subdivisions of the VCN (pVCN, aVCN, nerve root) by measuring the diameter and silhouette area of the cell bodies of the backfilled cells. The average diameter of T-stellate cells was 17.23 ± 2.42 μm, which is consistent with previous observations (Wu &

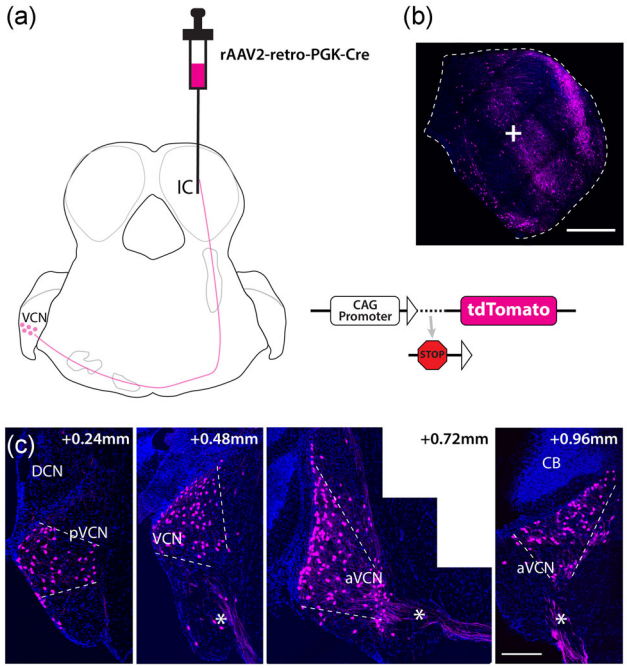

FIGURE 1 Labeling of T-stellate cells via viral injection. (a) Schematic of the experimental approach for identifying T-stellate cells. The rAAV2-retro-PKG-Cre vector was injected into the inferior colliculus (IC) of Ai14 mice to retrogradely infect T-stellate cells and allow the selective expression of tdTomato in infected neurons. (b) A small volume of injection (plus sign) results in a banding pattern of tdTomato expression (magenta) in the injected IC (outlined with dashed lines). DNA was counterstained with DAPI (blue). The stitched images were placed on black backgrounds for the purpose of visualizing the images all at the same orientation as the schematic in (a). (c) Distribution of tdTomato-labeled T-stellate cells in the contralateral cochlear nucleus (CN) from one experiment. Four coronal sections spanning the CN posterior-anterior axis showing tdTomato-labeled T-stellate cells (magenta) distributed along a band within both the posterior ventral CN (pVCN) and anterior VCN (outlined with white dashed lines). DNA was counterstained with DAPI (blue). Axons of T-stellate cells exit the CN via the ventral acoustic stria (asterisks). Scale bars in (b) = 500 μm, (c) = 200 μm. CB, cerebellum

Oertel, 1984), and the average somatic area was 158.72 ± 30.02 μm^2 (n = 645 from two animals). No statistically significant difference was observed between T-stellate cells distributed in different subdivisions (diameter: pVCN, 17.28 ± 2.19 μm vs. aVCN, 17.33 ± 2.51 μm vs. nerve root, 17.08 ± 2.57 μm, F = 0.625, ns, analysis of variance (ANOVA), somatic area: pVCN, 160.98 ± 29.85 μm^2 vs. aVCN, 159.97 ± 27.65 μm^2 vs. nerve root, 155.10 ± 32.30 μm^2, F = 2.35, p > .05, ANOVA).

3.2 | T-stellate cells synapse on other T-stellate cells

To identify the axonal boutons arising from the tdTomato-labeled axon collaterals of T-stellate cells in the VCN, we performed double immunostaining with anti-VGLUT2 and anti-PSD95 antibodies. VGLUT2 has been reported to be expressed in the terminals from T-stellate cells in the IC together with VGLUT1 (Ito & Oliver, 2010; Ito et al., 2009). In the VCN, we found that the axonal boutons of the local collaterals of tdTomato-labeled T-stellate cells also contain VGLUT2. Both terminal boutons (Figures 2a,b, 4, 7, and 8b) and en passant boutons (Figure 2c) are VGLUT2-positive. We also observed that, like the T-stellate terminals in the IC, the boutons that were positive for both VGLUT2 and tdTomato (subsequently referred to as VGLUT2/tdTomato boutons for simplicity) also contain VGLUT1 (Figure 3).

We measured the size of VGLUT2/tdTomato boutons that also contacted tdTomato-labeled T-stellate cells or their dendrites. The majority (83% of n = 141) of VGLUT2/tdTomato boutons are small (diameters < 3 μm). Large boutons with diameters of 4 to 5.4 μm were occasionally observed (n = 5). A portion of these VGLUT2/tdTomato boutons was found to contact the somata of T-stellate cells (Figure 2a,b; n = 60 on 47 cells from five animals), indicating that there were axosomatic synapses between the boutons and somata (Figure 2). Overlap of VGLUT2 and PSD95 at the appositions further supported the presence of the synapses. In some experiments, two or three boutons were observed to contact the soma of the same T-stellate cells (n = 10, Figure 2b). VGLUT2/tdTomato boutons were also found to contact the labeled dendrites of T-stellate cells (n = 81). Twenty-four of these boutons were found to contact 23 dendrites that could be traced back to their parent cell bodies at sites 2.33–78.54 μm away from the cell bodies. Twenty-one of them were less than 40-μm away (dendritic diameter = 2.266 ± 0.730 μm). Such observation indicated the presence of axodendritic synapses between T-stellate cells on proximal dendrites, which was further supported by the partial overlap of VGLUT2 and PSD95 puncta (Figure 4a). We also found VGLUT2/tdTomato boutons (n = 57) contacting segments (n = 49) of labeled T-stellate cell dendrites that could not be traced to their parent cell bodies. These dendrites had variable diameters. A total of 31/49 pieces of severed dendrites contacted by VGLUT2/tdTomato boutons were one standard deviation thinner than the average proximal diameter (< 1.536 μm), and 12 pieces of those dendrites were even two standard deviations thinner than the average proximal diameter (< 0.806 μm). No difference in size was observed between the VGLUT2/tdTomato boutons that contact somata and dendrites of T-stellate cells (p > .05).

3.3 | Ultrastructure of T-stellate cell synapse

We first wished to confirm that the synaptic coverage of our BDA backfilled T-stellate cells was similar to previous reports (Cant, 1981; Smith & Rhode, 1989). When terminal coverage of T-stellate cells is measured at the EM level, the somata of T-stellate cells are sparsely innervated (24.74 ± 11.16%, n = 6 from three animals), similar to that reported in cats (21%). To unequivocally identify synapses of T-stellate terminals on T-stellates, we performed electron microscopy of this BDA-labeled tissue. Our analysis confirmed the existence of synapses between retrogradely labeled T-stellate cells and revealed more details

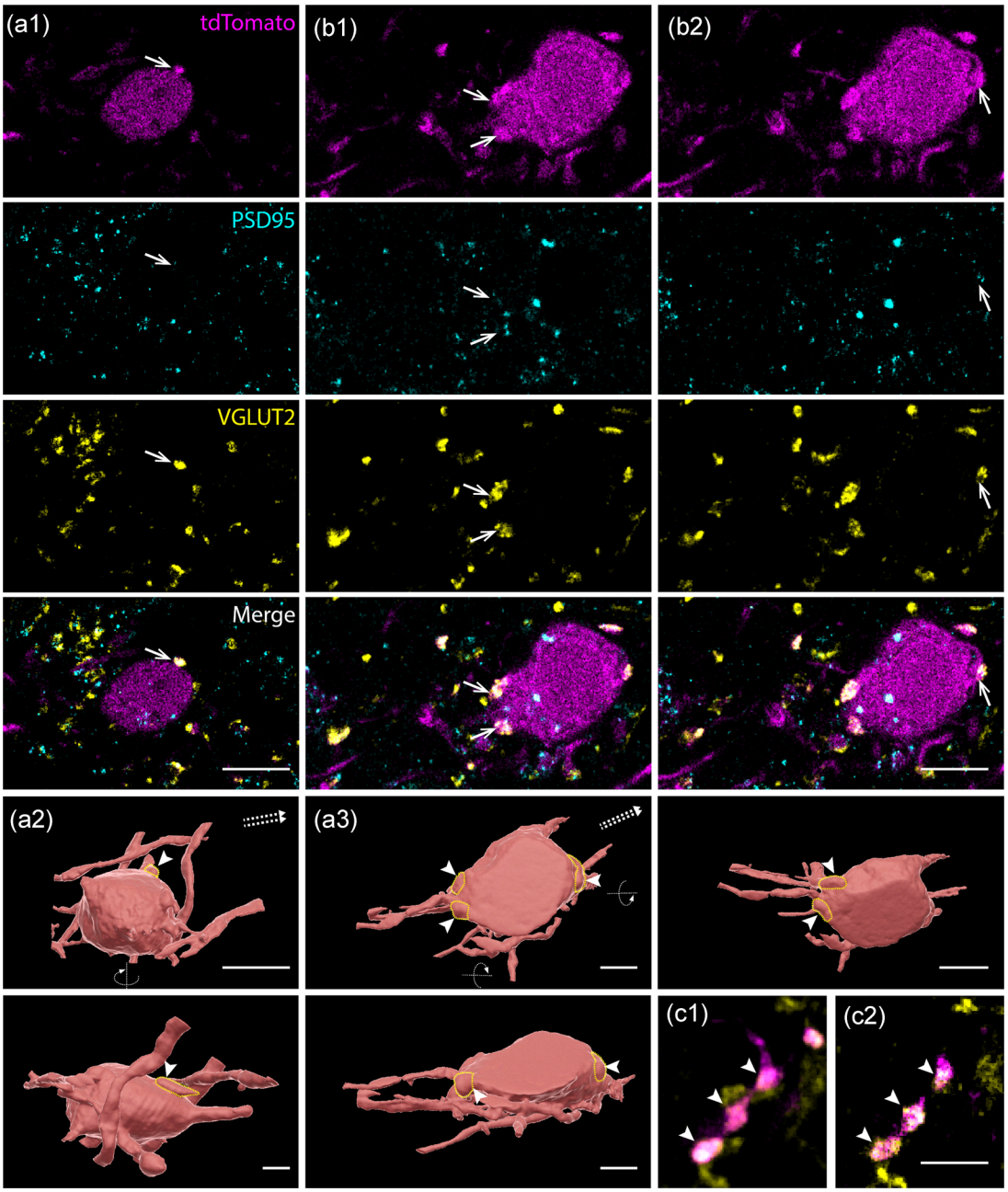

FIGURE 2 T-stellate cells synapsing on the soma of other T-stellate cells. (a) and (b), top row: two tdTomato-labeled T-stellate cells, one in (a1), and one in (b1) and (b2) at different levels in the z-stack, showing tdTomato-labeled boutons on their surface (arrows). These boutons are associated with PSD95 (second row, arrows) and coexpress VGLUT2 (third row, arrows). Images are merged in the fourth row. (a2) and (b3) are reconstructions of the tdTomato channel of the z-stacks of these cells from different angles of view. The orientations of the corresponding isofrequency laminae are indicated with double dashed arrows. The terminal boutons are outlined with yellow dashed lines and indicated by arrowheads. (c) The en passant boutons along the tdTomato (magenta)-labeled axon of a T-stellate cell, forming a "pearl-chain structure" and coexpressing VGLUT2 (yellow). (c1) is a 3-μm z-stack containing the structure, and (c2) is a single image from the stack. Scale bars in (a) and (b) = 10 μm, (c) = 5 μm

of the ultrastructure. Serial sections through retrogradely labeled T-stellate cells were examined, and in two cases, labeled boutons formed synapses on the soma of T-stellate cells (Figure 5). In addition, these boutons were found to make another synapse on small unlabeled nearby dendrites (Figure 5b2, b3, d1), making these multiple-synaptic boutons. T-stellate cell boutons were also found to synapse on severed pieces of BDA-labeled dendrites, confirming the axon-dendritic synapses between T-stellate cells ($n = 2$, Figure 6d).

We also found T-stellate cell terminals synapsing on unlabeled dendrites or spines that were not connected to their cell body of origin

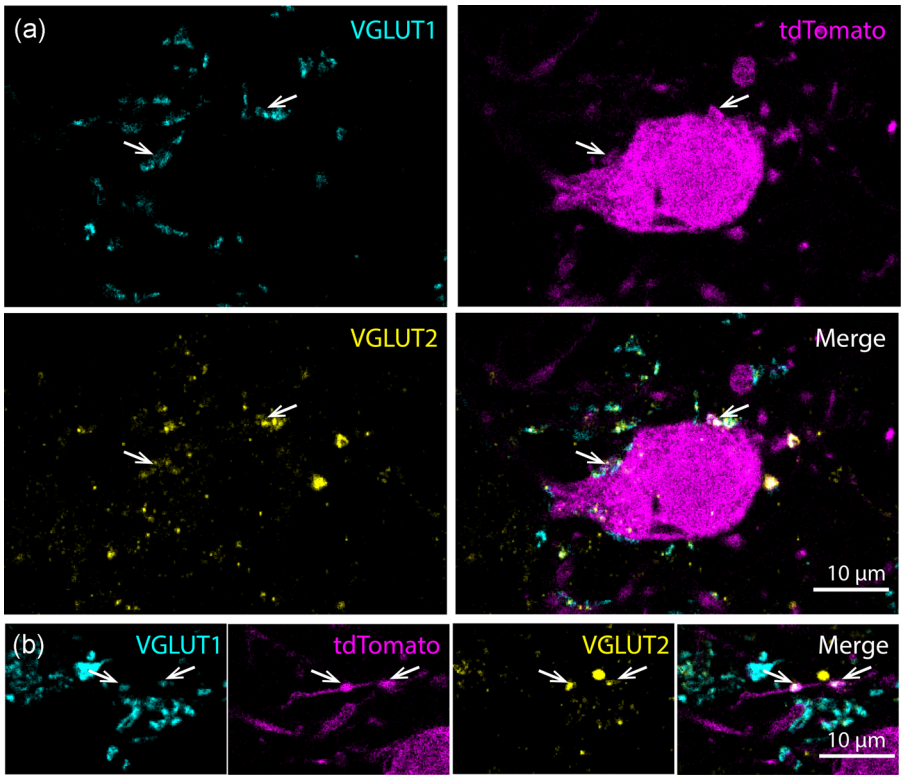

FIGURE 3 Vesicular glutamate transporter 1 and 2 (VGLUT1 and VGLUT2) are coexpressed in tdTomato-expressing T-stellate boutons. (a) Both VGLUT1 (cyan) and VGLUT2 (yellow) were found to be expressed in tdTomato-expressing (magenta) T-stellate boutons (arrows) apposed to the soma of T-stellate cells. Single optical sections of different sections are merged in the bottom right. (b) T-stellate boutons (arrows) that coexpress VGLUT1 (cyan) and VGLUT2 (yellow) were also found along the axon of T-stellate cells. Scale bars = 10 μm

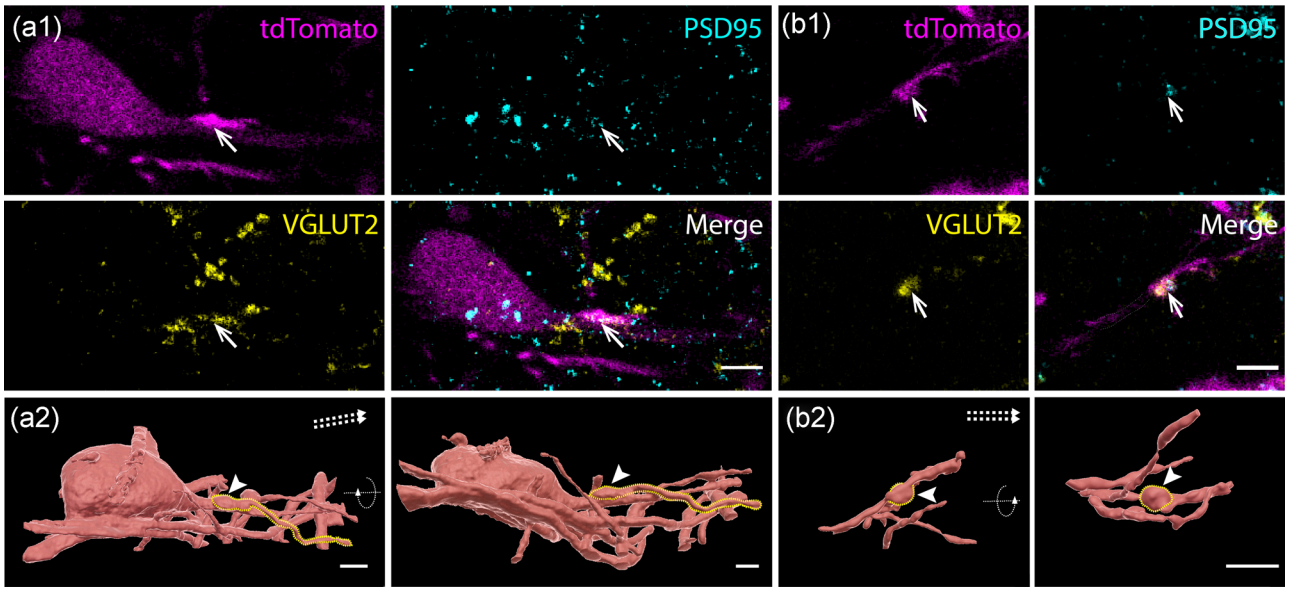

FIGURE 4 T-stellate cells synapse on the dendrites of other T-stellate cells. (a1) A tdTomato-labeled T-stellate cell with axonal swelling on its proximal dendrite (top left image, arrow) that was associated with PSD95 (top right image, arrow) and colabeled with VGLUT2 (bottom left image, arrow). Images are merged in the bottom right. (a2) Reconstruction of the z-stack of the tdTomato channel viewed from different angles to illustrate the bouton (arrowheads) located at the proximal dendrite. The bouton as well as the axon are outlined with yellow dashed lines. (b1) T-stellate bouton that coexpresses tdTomato (top left image, magenta) and VGLUT2 (lower left image, yellow) synapses on a piece of severed tdTomato-labeled dendrite. The swelling is also associated with PSD95 (upper right image, arrow). (b2) Reconstruction of the dendrite viewed from different angles. The bouton is outlined with yellow dashed lines and highlighted by arrowheads. In (a2) and (b2), the orientations of the corresponding isofrequency laminae are indicated with double dashed arrows. Scale bars = 5 μm

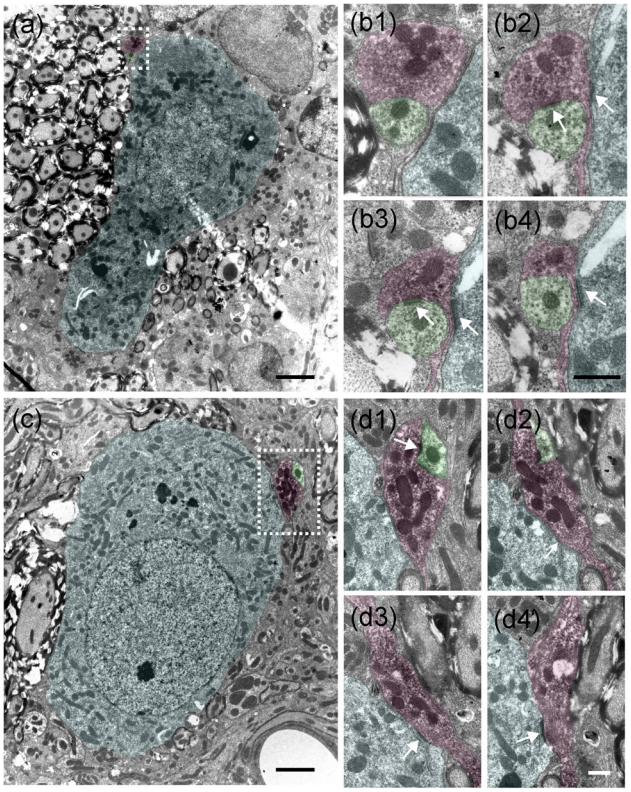

FIGURE 5 Electron micrographs of retrogradely labeled T-stellate cell boutons synapsing on other T-stellate cells. (a) A retrogradely labeled terminal bouton contacts the cell body of a labeled T-stellate cell with an infolded nuclear membrane. The bouton and cell body are highlighted in magenta and blue, respectively. (b) Consecutive sections through the labeled T-stellate cell terminal bouton (magenta) outlined with the dashed line in (a). The terminal synapses (arrows) on both the cell body and a nearby unlabeled dendrite (green). (c) Another retrogradely labeled bouton (magenta) contacts the cell body (blue) of a labeled T-stellate cell. (d) Consecutive sections through the T-stellate cell bouton outlined with the dashed line in (c). The bouton synapses (arrows) on both the soma of the T-stellate cell and an unlabeled dendrite (green). Scale bars in (a) and (c) = 2 μm, (b) and (d) = 500 nm

(n = 10 from three animals, Figure 6a–c). The large gross injections of BDA we made in these animals that filled a large portion of the IC presumably backfilled a large percentage of the T-stellate population. Thus, it is certainly a possibility that the unlabeled dendrites receiving labeled T-stellate terminals may belong to other cell types in the VCN. Strong evidence of this is provided below.

3.4 | T-stellate cells target glycinergic neurons

To test whether the labeled T-stellate cell terminals were targeting the glycinergic inhibitory neurons in the VCN, double immunostaining with anti-VGLUT2 and anti-glycine antibodies was performed on frozen VCN sections with tdTomato-labeled T-stellate cells. In two of the three animals, supplemental immunostaining with anti- TUBB3 antibody was performed to show the nuclei and morphology of neurons more clearly.

The glycine-labeled neurons were scattered throughout the VCN and had cell bodies of variable size. Axonal boutons from T-stellate cells that coexpressed tdTomato and VGLUT2 were apposed to the soma or proximal dendrite of glycine-labeled neurons (n = 174 from three animals, Figures 7 and 8b), indicating that T-stellate cells may, in addition to targeting other T-stellate cells, also target glycinergic neurons. Up to four axonal boutons were observed on the soma and proximal dendrite of individual neurons (Figure 7c).

The longest axis and somatic silhouette area of the glycinergic neurons receiving T-stellate inputs were measured and are illustrated in Figure 8a. We observed a bimodal distribution for both the diameter and somatic area for these glycinergic cells (marginal histograms in Figure 8a, diameter, $p < .02$; area, $p < .02$, dip test). The analyzed data sets show that the two modes are separated at 22.5–24 μm and 275–350 μm^2. In the scatter plot drawn from these two histograms, these data points clearly fall into two clusters whose means are more than three standard deviations away from each other along both axes. The small (olive green) and large (violet) glycinergic neurons were measured separately. The average diameter of small glycine neurons was 14.81± 2.79 μm (n = 168), and their somatic area was 124.03 ± 37.64 μm^2. The average diameter of large glycine neurons was 25.93 ± 1.51 μm (n = 6), and the somatic area was 383.84 ± 18.81 μm^2. This suggested that boutons from T-stellate cells are in association with at least two groups of glycinergic neurons, which may be distinguished by size. We speculate that these two groups correspond to the large glycinergic D-stellate cells that sparsely populate the VCN and project to the opposite cochlear nucleus (Doucet et al., 1999, 2009; Oertel et al., 1990; Smith et al., 2005) and the recently discovered small glycinergic L-stellate cells (Ngodup et al., 2020) that act as local interneurons and heavily populate the VCN.

4 | DISCUSSION

Using retrograde labeling methods, we evaluated the influence of T-stellate cells on those VCN cell types involved in the T-stellate circuitry, namely, other T-stellate cells and glycinergic L- and D-stellate cells (Figure 9). Retrograde BDA and viral labeling of T-stellate cells and their processes from the IC have verified the long-held notion (Ferragamo et al., 1998) that T-stellate terminals synapse on other T-stellate cells both at the cell body and dendritic levels. Our evidence using viral backfilling indicates that the T-stellate axon terminals from one T-stellate cell in a given isofrequency lamina can have a synaptic influence on other T-stellate cells within the same lamina. These experiments also indicate that the T-stellate terminals can be identified by their couse of both vesicle glutamate transporters VGLUT1 and 2 and their colocalization with PSD95, similar to what has been reported for T-stellate terminals in the IC (Ito & Oliver, 2010; Olthof et al., 2019). In addition, T-stellate terminals were also seen synapsing on the cell bodies and dendrites of two size categories of glycinergic VCN cells, small and large. The sizes and relative numbers of these cells indicate

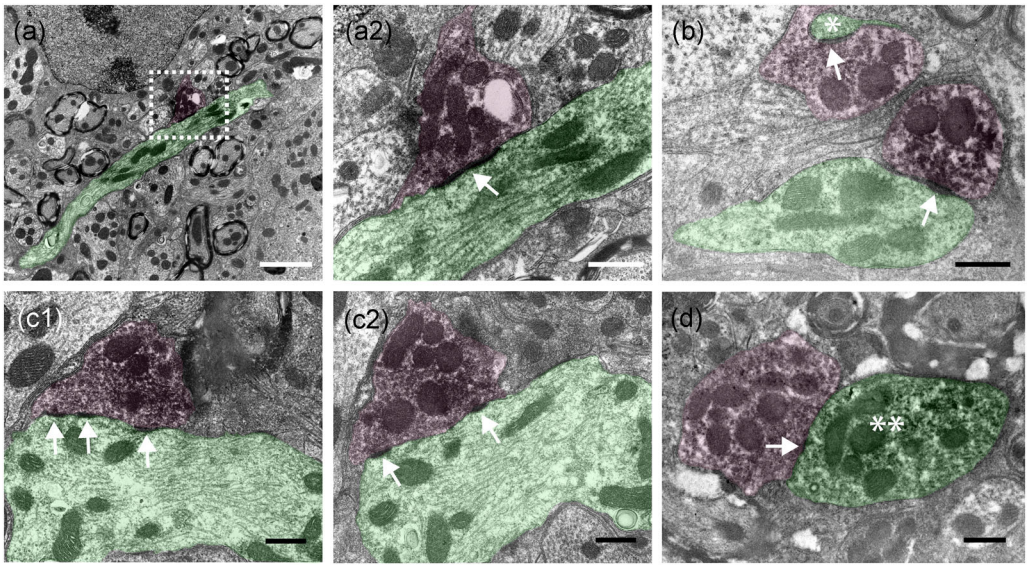

FIGURE 6 Electron micrographs of retrogradely labeled T-stellate cell terminals synapsing on unlabeled dendrites. (a) A labeled terminal bouton synapse (outlined with dotted line) on a long piece of unlabeled dendrite (green). (a2) Enlargement of the outlined area in a1 showing synaptic specialization (arrow). (b-c) Other examples of T-stellate axon terminals (magenta) synapsing (arrows) on unlabeled dendrites (green) and a spine (asterisk). (d) Labeled terminal synapse (arrow) on a labeled dendrite (asterisks). Scale bars in (a1) = 2 μm, (a2) and (b)-(d) = 500 nm

that they are likely the D- and L-stellate categories of glycinergic VCN neurons that provide inhibitory inputs back onto T-stellate cells. These connections were seen in the viral labeling experiments, again indicating that the interactions occur between cells that are within the same isofrequency lamina.

Previous evidence indicated that T-stellate inputs to other T-stellate cells might be prevalent and an important component of their excitatory input. In brain slices where many connections are cut, late, polysynaptic EPSPs, presumably arising from T-stellate terminals, were consistently observed following auditory nerve shock in over 80% of T-stellate cells (Ferragamo et al., 1998). Other studies (Cant, 1981; Smith & Rhode, 1989) have shown that auditory nerve terminals contain large round vesicles, while T-stellate terminals contain small round vesicles. Many of these auditory nerve terminals from a small number of ANFs (five to six in mouse, Ferragamo et al., 1998) are located primarily on the dendritic tree of T-stellate cells (Smith & Rhode, 1989). In contrast, we noted that at least 58% of the T-stellate terminals (82/141) synapse close to or on the cell body of other T-stellate cells. Of the 141 virally labeled T-stellate terminals seen on virally labeled T-stellate cell bodies or dendrites, 43% (60/141) were found on the cell body. Of the other 81 terminating on dendrites, 22 (27%) were located on proximal dendrites within 40 μm of the connected T-stellate cell body, and 20 (25%) were located on severed pieces with compatible diameters. Thus, it would seem that the T-stellate input may be of considerable importance to the response features of other T-stellate cells even under normal circumstances.

All of this would imply that T-stellate cells are unique among the excitatory VCN projection neuron classes in that they are influenced by multiple inhibitory cell types in the CN and, in turn, talk back to those same cell types forming intrinsic networks within the CN. This is in direct contrast to the other two excitatory VCN projection neurons, bushy and octopus cells. Bushy cells receive several inputs from local VCN cell types and can be modulated by external inputs (see Kuenzel, 2019), but they have no local axon collaterals to feed back onto and excite these local sources of inputs (Smith et al., 1991, 1993). Octopus cell axons have local axon collaterals with unknown cellular destinations (Friauf & Ostwald, 1988; Golding et al., 1995; Smith et al., 2005), but the octopus cell and the octopus cell area have no known excitatory inputs other than the auditory nerve and are devoid of any inhibitory terminals, with no inhibitory post-synaptic potentials (IPSPs) ever reported from in vivo or in vitro intracellular octopus cell recordings (Oertel, personal communication, 2019; Ostapoff et al., 1994; Rhode et al., 1983)

The demonstration of connections between T stellate cells, particularly in an isofrequency lamina, has significant implications for the way the brain stem processes complex acoustic information like vowels with their multiple spectral peaks at formant frequencies. Potentiation of connections between T stellate cells within an isofrequency lamina could act as a form of variable central gain control (Coomber et al., 2015). If present within an isofrequency lamina, such interconnects might create "functional networks/units" at the formant frequencies and serve to upregulate these loudest components, that is, the formants and enhance the encoding of vowel spectral peaks. Such enhancement has been reported in vivo, in particular by the "chopper response" population (Blackburn & Sachs, 1990), which corresponds to T-stellate cells (see Oertel et al., 2011). A possible mechanism for this local potentiation is the activation of the nitric oxide pathway, which is present in T-stellate cells. When activated, either by (1) stepping the membrane potential to +20 mV while repetitively activating another T-stellate cell, or (2) bath application of PAPA NONOate, a nitric oxide

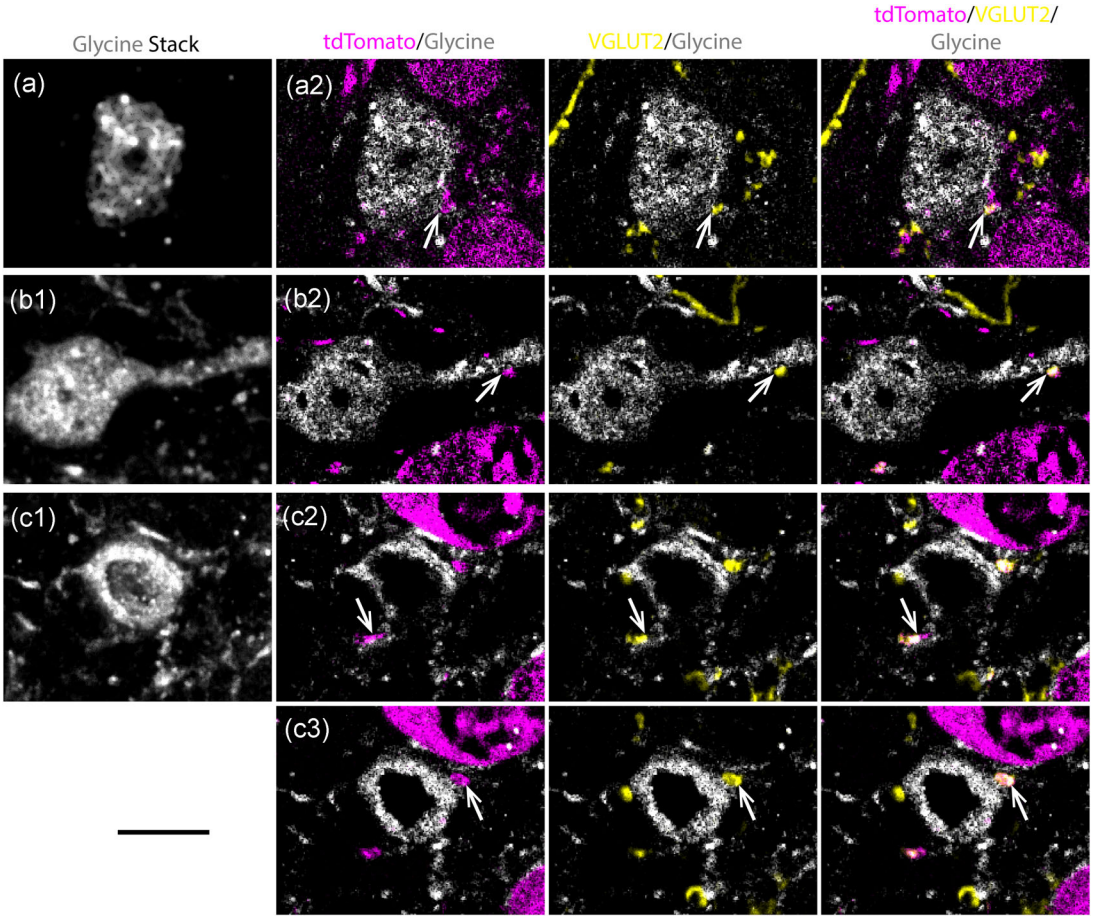

FIGURE 7 Small glycinergic neurons in association with puncta from T-stellate cells. (a1), (b1) and (c1) Projections of z-stacks containing the small glycinergic neurons. (a2) Images of the small glycinergic neuron (white) from a1 with a bouton (arrows) coexpressing tdTomato (left panel, magenta) and VGLUT2 (middle panel, yellow) on soma. (b2) Images of another small glycinergic neuron (white) from b1 with a bouton (arrows) coexpressing tdTomato (left panel, magenta) and VGLUT2 (middle panel, gold) on a proximal dendrite. (c2-c3) Images of different sections of the third small glycinergic neuron (white) from c1 with puncta (arrows) coexpressing tdTomato (left panel, magenta) and VGLUT2 (middle panel, yellow) on both soma (c2, arrows) and proximal dendrites (c3, arrows). The left and middle panels were merged into the right panel. Scale bar = 10 μm

donor (Cao, Lin, Sugden, et al., 2019), or (3) repetitive stimulation of the auditory nerve input (Cao & Oertel, 2020), T-stellate excitatory inputs are amplified. Of the three excitatory VCN projection neurons, that is, T-stellate, octopus and bushy cells appear to be unique to the T-stellate cells.

It has also been shown that activation of the nitric oxide pathway is capable of upregulating the response features of one of the glycinergic cell types in the T-stellate network, the D-stellate cell (Cao, Lin, Oertel, 2019). Voltage clamping these cells to depolarized levels causes them to synthesize and release NO, which generates an increased excitatory input to the voltage clamped cell, likely the T-stellate inputs to these cells. The activation is NMDA- and NO synthesis-dependent. It will be interesting to see if the other cell types in this circuit provide inhibition to the T-stellate cells., that is, L-stellate (Ngodup et al., 2020) and tuberculoventral cells (Wickesberg et al., 1991) are also NO sensitive. One possible reason for such an increased excitatory input to one or more of the inhibitory cells in the T-stellate circuit would be to maintain a balance in the excitatory and inhibitory inputs to T-stellate cells, thus allowing the upregulation of this excitatory CN projection neuron but preventing a runaway output of the same population. Another possible reason would be to increase the peak-to-trough rate in spectrum representation in T-stellate cells via upregulation of the off-BF (best frequency) inhibition. "Off-BF" input has been found to suppress the firing rate of "on-BF" chopper units (Blackburn & Sachs, 1992), whose mechanism could be the "wideband" or "narrowband" inhibition from glycinergic neurons. Blocking glycinergic inhibition was shown to rescue the firing rate (Gai & Carney, 2008).

This NO-mediated potentiation mechanism has also been implicated in the generation of salicylate-induced (Zheng et al., 2006) or noise-induced (Coomber et al., 2014, 2015; Hockley et al., 2020) tinnitus and presbycusis. In noise-induced hearing loss, there is an upregulation of NO synthesis presumably to compensate for the loss of auditory nerve input and to facilitate an enhanced response to the remaining input. Somehow, this upregulation is presumed to be

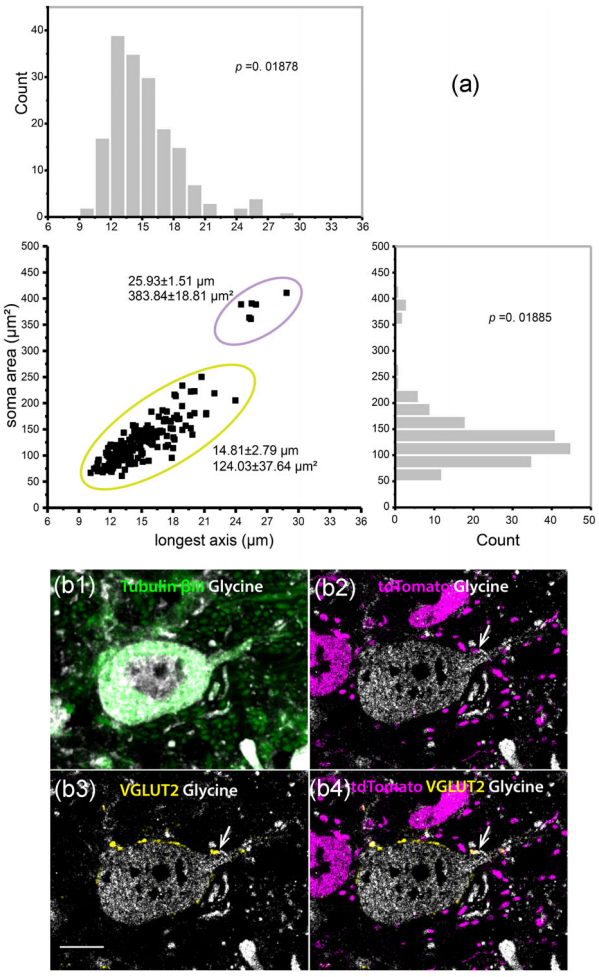

FIGURE 8 Puncta from T-stellate cells are in contact with more than one size group of glycinergic neurons. (a) Scatterplot with marginal histograms of the longest axis vs somatic area of the glycinergic neurons, which are associated with puncta from T-stellate cells. Each isolated black square in the 2D plot corresponds to one glycinergic neuron. The clusters correspond to small (olive green oval, average longest axis of soma = 14.81 ± 2.79 μm, average somatic area = 124.03 ± 37.64 μm^2) and large (violet oval, average longest axis of soma = 25.93 ± 1.51 μm, average somatic area = 383.84 ± 18.81 μm^2) glycinergic neurons, respectively. The marginal histograms on the top and side are projections of the dot plot to a single axis. Hartigan's dip test was used to test unimodality (both $p < .05$, dip test). (b) Confocal micrographs of a large glycinergic neuron in association with puncta from a T-stellate cell. b1 is the z-stack projection showing a large glycinergic neuron (glycine, white; Tubulin βIII, green, diameter = 24.45 μm). (b2–b4) are images of a single section from the stack containing a bouton (arrow) coexpressing tdTomato (b2, magenta) and VGLUT2 (b3, yellow), which is in association with the large glycinergic neuron (white). All channels are merged in (b4). Scale bar = 10 μm

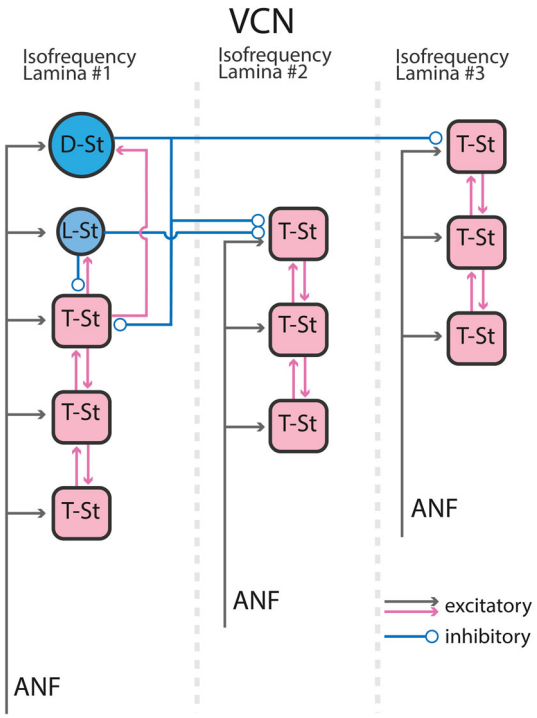

FIGURE 9 Summary of T-stellate circuitry in the VCN. Auditory nerve fibers excite excitatory T-stellate cells (T-St) and inhibitory D-stellate (D-St) and L-stellate (L-St) cells. Multiple T-stellate cells are interconnected with each other monosynaptically, likely within an isofrequency lamina. T-stellate cells also make local excitatory synaptic contacts on L-stellate cells, which probably provide narrow side band inhibitory inputs back onto T-stellate cells in the same and immediately adjacent lamina. T-stellates also make local excitatory synaptic contacts on D-stellate cells, which provide wide-band inhibitory inputs back onto T-stellates over multiple laminae

imperfect, leading to a shift in the balance of excitation and inhibition, described above, that favors excitation and leads to increased spontaneous activity in the absence of auditory input (tinnitus) and/or an increased driven rate at higher stimulus intensities (presbycusis) in certain CN projection neurons (Schrode et al., 2018).

In salicylate-induced tinnitus, a significant increase in the number of nNOS-expressing VCN principal neurons has also been noted (Zheng et al., 2006), and as a result, there is thought to be a progressive amplification of the neural response to sound as one ascends to the IC, medial geniculate, and auditory cortex (for review, see Salvi et al., 2021). Interestingly, one recent study of salicylate-induced tinnitus points to the T-stellate input to the IC as the instigator of this amplification (Olthof et al., 2021). In tinnitus generated by systemic application of salicylate, extracellular recordings from cells in the ICC showed an increase in both spontaneous and driven firing rates that was blocked by an NOS inhibitor injected into the IC. However, direct application of salicylate only to the ICC did not generate an increased response, indicating that salicylate acts on cells providing excitatory synaptic inputs to the ICC and that these synapses are capable of activating NO in the IC. Previous work from their lab showed that terminals in the ICC likely arising from T-stellate axons have the postsynaptic machinery required for NO synthesis (Olthof et al., 2019).

Together, our work demonstrated anatomical evidence that T-stellate cells directly interconnect with each other within an intrinsic network but also send inputs to inhibitory neurons. This circuitry may help maintain a delicate excitatory and inhibitory balance and provide

a neuroanatomical basis for acoustic information processing involving not only single but also multiple "functional networks/units" of T-stellates across frequencies. Disturbance of the circuitry may be related to the generation of tinnitus.

ACKNOWLEDGMENTS

This work was supported by National Institutes of Health grant NIH R01DC016861. We would like to thank Dr. C. L. Zhang and Dr. D. C. Joshi for technical assistance. We are grateful to Dr. M. V. Jones and Dr. L. O. Trussell for their helpful discussions. Finally, this article is dedicated to the memory of a dear friend, colleague, and mentor, Dr. Donata Oertel.

CONFLICT OF INTEREST

The authors declare that there are no potential sources of conflict of interest.

DATA AVAILABILITY STATEMENT

Data that support the findings of this study are available from the corresponding author upon reasonable request.

ORCID

Lin Lin https://orcid.org/0000-0002-9640-0687
Jay Campbell https://orcid.org/0000-0002-9916-2055
Donata Oertel https://orcid.org/0000-0001-8416-7470
Philip H. Smith https://orcid.org/0000-0003-3841-7031

REFERENCES

Adams, J. C. (1979). Ascending projections to the inferior colliculus. *The Journal of Comparative Neurology*, *183*(3), 519–538. https://doi.org/10.1002/cne.901830305

Adams, J. C. (1983). Multipolar cells in the ventral cochlear nucleus project to the dorsal cochlear nucleus and the inferior colliculus. *Neuroscience Letters*, *37*(3), 205––208. https://doi.org/10.1016/0304-3940(83)90431-7

Bäurle, J., Helmchen, C., & Grüsser-Cornehls, U. (1997). Diverse effects of Purkinje cell loss on deep cerebellar and vestibular nuclei neurons in Purkinje cell degeneration mutant mice: A possible compensatory mechanism. *The Journal of Comparative Neurology*, *384*(4), 580–596. https://doi.org/10.1002/(SICI)1096-9861(19970811)384:4⟨580::AID-CNE7⟩3.0.CO;2-Z

Blackburn, C. C., & Sachs, M. B. (1990). The representations of the steady-state vowel sound/e/in the discharge patterns of cat anteroventral cochlear nucleus neurons. *Journal of Neurophysiology*, *63*(5), 1191–1212. https://doi.org/10.1152/jn.1990.63.5.1191

Blackburn, C. C., & Sachs, M. B. (1992). Effects of OFF-BF tones on responses of chopper units in the ventral cochlear nucleus. I. Regularity and temporal adaptation patterns. *Journal of Neurophysiology*, *68*(1), 124–143. https://doi.org/10.1152/jn.1992.68.1.124

Brawer, J. R., Kent Morest, D., & Kane, E. C. (1974). The neuronal architecture of the cochlear nucleus of the cat. *The Journal of Comparative Neurology*, *155*(3), 251––299. https://doi.org/10.1002/cne.901550302

Campagnola, L., & Manis, P. B. (2014). A map of functional synaptic connectivity in the mouse anteroventral cochlear nucleus. *The Journal of Neuroscience*, *34*(6), 2214–2230. https://doi.org/10.1523/JNEUROSCI.4669-13.2014

Cant, N. B. (1981). The fine structure of two types of stellate cells in the anterior division of the anteroventral cochlear nucleus of the cat. *Neuroscience*, *6*(12), 2643–2655. https://doi.org/10.1016/0306-4522(81)90109-3

Cant, N. B. (1982). Identification of cell types in the anteroventral cochlear nucleus that project to the inferior colliculus. *Neuroscience Letters*, *32*(3), 241–246. https://doi.org/10.1016/0304-3940(82)90300-7

Cao, X. -J., Lin, L., & Oertel, D. (2019). Nitric oxide-mediated plasticity in inhibitory neurons of the ventral cochlear nucleus. *42nd Midwinter Meeting of the Association for Research in Otolaryngology*, Baltimore, MD.

Cao, X. -J., Lin, L., Sugden, A. U., Connors, B. W., & Oertel, D. (2019). Nitric oxide-mediated plasticity of interconnections between t-stellate cells of the ventral cochlear nucleus generate positive feedback and constitute a central gain control in the auditory system. *The Journal of Neuroscience*, *39*(31), 6095–6107. https://doi.org/10.1523/JNEUROSCI.0177-19.2019

Cao, X. -J., & Oertel, D. (2020). Stimulation of auditory nerve fibers with trains of shocks engages excitatory interconnections between T Stellate cells of the ventral cochlear nucleus. *43rd Midwinter Meeting of the Association for Research in Otolaryngology*, San José, CA.

Coomber, B., Berger, J. I., Kowalkowski, V. L., Shackleton, T. M., Palmer, A. R., & Wallace, M. N. (2014). Neural changes accompanying tinnitus following unilateral acoustic trauma in the guinea pig. *European Journal of Neuroscience*, *40*(2), 2427–2441. https://doi.org/10.1111/ejn.12580

Coomber, B., Kowalkowski, V. L., Berger, J. I., Palmer, A. R., & Wallace, M. N. (2015). Modulating central gain in tinnitus: Changes in nitric oxide synthase in the ventral cochlear nucleus. *Frontiers in Neurology*, *6*, 53. https://doi.org/10.3389/fneur.2015.00053

Darrow, K. N., Benson, T. E., & Brown, M. C. (2012). Planar multipolar cells in the cochlear nucleus project to medial olivocochlear neurons in mice. *The Journal of Comparative Neurology*, *520*(7), 1365–1375. https://doi.org/10.1002/cne.22797

Doucet, J. R., Lenihan, N. M., & May, B. J. (2009). Commissural neurons in the rat ventral cochlear nucleus. *Journal of the Association for Research in Otolaryngology: JARO*, *10*(2), 269–280. https://doi.org/10.1007/s10162-008-0155-6

Doucet, J. R., Ross, A. T., Gillespie, M. B., & Ryugo, D. K. (1999). Glycine immunoreactivity of multipolar neurons in the ventral cochlear nucleus that project to the dorsal cochlear nucleus. *The Journal of Comparative Neurology*, *408*(4), 515–531. https://doi.org/10.1002/(SICI)1096-9861(19990614)408:4⟨515::AID-CNE6⟩3.0.CO;2-O

Doucet, J. R., & Ryugo, D. K. (1997). Projections from the ventral cochlear nucleus to the dorsal cochlear nucleus in rats. *The Journal of Comparative Neurology*, *385*(2), 245–264. https://doi.org/10.1002/(sici)1096-9861(19970825)385:2⟨245::aid-cne5⟩3.0.co;2-1

Ferragamo, M. J., Golding, N. L., & Oertel, D. (1998). Synaptic inputs to stellate cells in the ventral cochlear nucleus. *Journal of Neurophysiology*, *79*(1), 51–63. https://doi.org/10.1152/jn.1998.79.1.51

Friauf, E., & Ostwald, J. (1988). Divergent projections of physiologically characterized rat ventral cochlear nucleus neurons as shown by intra-axonal injection of horseradish peroxidase. *Experimental Brain Research*, *73*(2), 263–284. https://doi.org/10.1007/BF00248219

Gai, Y., & Carney, L. H. (2008). Influence of inhibitory inputs on rate and timing of responses in the anteroventral cochlear nucleus. *Journal of Neurophysiology*, *99*(3), 1077–1095. https://doi.org/10.1152/jn.00708.2007

Golding, N. L., Robertson, D., & Oertel, D. (1995). Recordings from slices indicate that octopus cells of the cochlear nucleus detect coincident firing of auditory nerve fibers with temporal precision. *The Journal of Neuroscience*, *15*(4), 3138–3153. https://doi.org/10.1523/JNEUROSCI.15-04-03138.1995

Hockley, A., Berger, J. I., Palmer, A. R., & Wallace, M. N. (2020). Nitric oxide increases gain in the ventral cochlear nucleus of guinea pigs with tinnitus. *The European Journal of Neuroscience*, *52*(9), 4057–4080. https://doi.org/10.1111/ejn.14913

Ito, T., Bishop, D. C., & Oliver, D. L. (2009). Two classes of GABAergic neurons in the inferior colliculus. *The Journal of Neuroscience*, *29*(44), 13860–13869. https://doi.org/10.1523/JNEUROSCI.3454-09.2009

Ito, T., & Oliver, D. L. (2010). Origins of glutamatergic terminals in the inferior colliculus identified by retrograde transport and expression of the VGLUT1 and VGLUT2 genes. *Frontiers in Neuroanatomy*, *4*, 135. https://doi.org/10.3389/fnana.2010.00135

Kalloniatis, M., & Fletcher, E. L. (1993). Immunocytochemical localization of amino acid neurotransmitters in the chicken retina. *The Journal of Comparative Neurology*, *336*(2), 174–193. https://doi.org/10.1002/cne.903360203

Kuenzel, T. (2019). Modulatory influences on time-coding neurons in the ventral cochlear nucleus. *Hearing Research*, *384*, 107824. https://doi.org/10.1016/j.heares.2019.107824

Laudanski, J., Coombes, S., Palmer, A. R., & Sumner, C. J. (2010). Mode-locked spike trains in responses of ventral cochlear nucleus chopper and onset neurons to periodic stimuli. *Journal of Neurophysiology*, *103*(3), 1226–1237. https://doi.org/10.1152/jn.00070.2009

Lee, M. K., Rebhun, L. I., & Frankfurter, A. (1990). Posttranslational modification of class III beta-tubulin. *Proceedings of the National Academy of Sciences*, *87*(18), 7195–7199. https://doi.org/10.1073/pnas.87.18.7195

Madisen, L., Zwingman, T. A., Sunkin, S. M., Oh, S. W., Zariwala, H. A., Gu, H., Ng, L. L., Palmiter, R. D., Hawrylycz, M. J., Jones, A. R., Lein, E. S., & Zeng, H. (2010). A robust and high-throughput Cre reporting and characterization system for the whole mouse brain. *Nature Neuroscience*, *13*(1), 133–140. https://doi.org/10.1038/nn.2467

May, B. J., Prell, G. S., & Sachs, M. B. (1998). Vowel representations in the ventral cochlear nucleus of the cat: Effects of level, background noise, and behavioral state. *Journal of Neurophysiology*, *79*(4), 1755–1767. https://doi.org/10.1152/jn.1998.79.4.1755

Murao, N., Yokoi, N., Honda, K., Han, G., Hayami, T., Gheni, G., Takahashi, H., Minami, K., & Seino, S. (2017). Essential roles of aspartate aminotransferase 1 and vesicular glutamate transporters in β-cell glutamate signaling for incretin-induced insulin secretion. *Plos One*, *12*(11), e0187213. https://doi.org/10.1371/journal.pone.0187213

Ngodup, T., Romero, G. E., & Trussell, L. O. (2020). Identification of an inhibitory neuron subtype, the L-stellate cell of the cochlear nucleus. *eLife*, *9*, 1–40. https://doi.org/10.7554/eLife.54350

Oertel, D. (1984). Cells in the anteroventral cochlear nucleus are insensitive to l-glutamate and l-aspartate; excitatory synaptic responses are not blocked by d-α-aminoadipate. *Brain Research*, *30*(2), 213–220. https://doi.org/10.1016/0006-8993(84)90233-6

Oertel, D., Wright, S., Cao, X. -J., Ferragamo, M., & Bal, R. (2011). The multiple functions of T stellate/multipolar/chopper cells in the ventral cochlear nucleus. *Hearing Research*, *276*(1-2), 61–69. https://doi.org/10.1016/j.heares.2010.10.018

Oertel, D., Wu, S. H., Garb, M. W., & Dizack, C. (1990). Morphology and physiology of cells in slice preparations of the posteroventral cochlear nucleus of mice. *The Journal of Comparative Neurology*, *295*(1), 136–154. https://doi.org/10.1002/cne.902950112

Oliver, D. L. (1987). Projections to the inferior colliculus from the anteroventral cochlear nucleus in the cat: Possible substrates for binaural interaction. *The Journal of Comparative Neurology*, *264*(1), 24–46. https://doi.org/10.1016/S0378-5955(96)00121-9

Olthof, B. M. J., Gartside, S. E., & Rees, A. (2019). The puncta of neuronal nitric oxide synthase (nNOS) mediate NMDA receptor signaling in the auditory midbrain. *The Journal of Neuroscience*, *39*(5), 876–887. https://doi.org/10.1523/JNEUROSCI.1918-18.2018

Olthof, B. M. J., Lyzwa, D., Gartside, S. E., & Rees, A. (2021). Nitric oxide signaling underlies salicylate-induced increases in neuronal firing in the inferior colliculus: A central mechanism of tinnitus? *bioRxiv*, https://doi.org/10.1101/2021.05.14.444151

Osen, K. K. (1969). Cytoarchitecture of the cochlear nuclei in the cat. *The Journal of Comparative Neurology*, *136*(4), 453–484. https://doi.org/10.1002/cne.901360407

Ostapoff, E. M., Feng, J. J., & Morest, D. K. (1994). A physiological and structural study of neuron types in the cochlear nucleus. II. Neuron types and their structural correlation with response properties. *The Journal of Comparative Neurology*, *346*(1), 19–42. https://doi.org/10.1002/cne.903460103

Palmer, A. R., Jiang, D., & Marshall, D. H. (1996). Responses of ventral cochlear nucleus onset and chopper units as a function of signal bandwidth. *Journal of Neurophysiology*, *75*(2), 780–794. https://doi.org/10.1152/jn.1996.75.2.780

Rhode, W. S., & Greenberg, S. (1994). Encoding of amplitude modulation in the cochlear nucleus of the cat. *Journal of Neurophysiology*, *71*(5), 1797–1825.

Rhode, W. S., Oertel, D., & Smith, P. H. (1983). Physiological response properties of cells labeled intracellularly with horseradish peroxidase in the cat ventral cochlear nucleus. *The Journal of Comparative Neurology*, *213*(4), 448–463. https://doi.org/10.1002/cne.902130408

Ryugo, D. K., Willard, F. H., & Fekete, D. M. (1981). Differential afferent projections to the inferior colliculus from the cochlear nucleus in the albino mouse. *Brain Research*, *210*(1-2), 342–349. https://doi.org/10.1016/0006-8993(81)90907-0

R Core Team. (2020). R: A language and environment for statistical computing, Vienna, Austria.

Salvi, R., Auerbach, B. D., Lau, C., Chen, Y. -C., Manohar, S., Liu, X., Ding, D., & Chen, G. -D. (2021). Functional neuroanatomy of salicylate-and noise-induced tinnitus and hyperacusis. *Current Topics in Behavioral Neurosciences*, *51*, 133–160. https://doi.org/10.1007/7854_2020_156

Schofield, B. R., & Cant, N. B. (1996). Projections from the ventral cochlear nucleus to the inferior colliculus and the contralateral cochlear nucleus in guinea pigs. *Hearing Research*, *102*(1-2), 1–14. https://doi.org/10.1016/S0378-5955(96)00121-9

Schrode, K. M., Muniak, M. A., Kim, Y. -H., & Lauer, A. M. (2018). Central compensation in auditory brainstem after damaging noise exposure. *eNeuro*, *5*(4), ENEURO.0250-18.2018. https://doi.org/10.1523/ENEURO.0250-18.2018

Sento, S., & Ryugo, D. K. (1989). Endbulbs of held and spherical bushy cells in cats: Morphological correlates with physiological properties. *The Journal of Comparative Neurology*, *280*(4), 553–562. https://doi.org/10.1002/cne.902800406

Shannon, R. V., Zeng, F. G., Kamath, V., Wygonski, J., & Ekelid, M. (1995). Speech recognition with primarily temporal cues. *Science*, *270*(5234), 303–304. https://doi.org/10.1126/science.270.5234.303

Smith, P. H., Joris, P. X., Carney, L. H., & Yin, T. C. (1991). Projections of physiologically characterized globular bushy cell axons from the cochlear nucleus of the cat. *The Journal of Comparative Neurology*, *304*(3), 387–407. https://doi.org/10.1002/cne.903040305

Smith, P. H., Joris, P. X., & Yin, T. C. (1993). Projections of physiologically characterized spherical bushy cell axons from the cochlear nucleus of the cat: Evidence for delay lines to the medial superior olive. *The Journal of Comparative Neurology*, *331*(2), 245–260. https://doi.org/10.1002/cne.903310208

Smith, P. H., Massie, A., & Joris, P. X. (2005). Acoustic stria: Anatomy of physiologically characterized cells and their axonal projection patterns. *The Journal of Comparative Neurology*, *482*(4), 349–371. https://doi.org/10.1002/cne.20407

Smith, P. H., & Rhode, W. S. (1989). Structural and functional properties distinguish two types of multipolar cells in the ventral cochlear nucleus. *The Journal of Comparative Neurology*, *282*(4), 595–616. https://doi.org/10.1002/cne.902820410

Tervo, D. G. R., Hwang, B. -Y., Viswanathan, S., Gaj, T., Lavzin, M., Ritola, K. D., Lindo, S., Michael, S., Kuleshova, E., Ojala, D., Huang, C. -C., Gerfen, C. R., Schiller, J., Dudman, J. T., Hantman, A. W., Looger, L. L., Schaffer, D. V., & Karpova, A. Y. (2016). A designer AAV variant permits efficient retrograde access to projection neurons. *Neuron*, *92*(2), 372–382. https://doi.org/10.1016/j.neuron.2016.09.021

Wickesberg, R. E., & Oertel, D. (1988). Tonotopic projection from the dorsal to the anteroventral cochlear nucleus of mice. *The Journal of Comparative Neurology*, *268*(3), 389–399. https://doi.org/10.1002/cne.902680308

Wickesberg, R. E., Whitlon, D., & Oertel, D. (1991). Tuberculoventral neurons project to the multipolar cell area but not to the octopus cell area of the posteroventral cochlear nucleus. *The Journal of Comparative Neurology*, *313*(3), 457–468. https://doi.org/10.1002/cne.903130306

Wu, S. H., & Oertel, D. (1984). Intracellular injection with horseradish peroxidase of physiologically characterized stellate and bushy cells in slices of mouse anteroventral cochlear nucleus. *The Journal of Neuroscience*, *4*(6), 1577–1588. https://doi.org/10.1523/JNEUROSCI.04-06-01577.1984

Xie, R., & Manis, P. B. (2013). Target-specific IPSC kinetics promote temporal processing in auditory parallel pathways. *The Journal of Neuroscience*, *33*(4), 1598–1614. https://doi.org/10.1523/JNEUROSCI.2541-12.2013

Xie, R., & Manis, P. B. (2014). GABAergic and glycinergic inhibitory synaptic transmission in the ventral cochlear nucleus studied in VGAT channelrhodopsin-2 mice. *Frontiers in Neural Circuits*, *8*, 84. https://doi.org/10.3389/fncir.2014.00084

Zhang, X. -Y., Dou, Y. -N., Yuan, L., Li, Q., Zhu, Y. -J., Wang, M., & Sun, Y. -G. (2020). Different neuronal populations mediate inflammatory pain analgesia by exogenous and endogenous opioids. *eLife*, *9*, 1–28. https://doi.org/10.7554/eLife.55289

Zheng, Y., Seung Lee, H., Smith, P. F., & Darlington, C. L. (2006). Neuronal nitric oxide synthase expression in the cochlear nucleus in a salicylate model of tinnitus. *Brain Research*, *1123*(1), 201–206. https://doi.org/10.1016/j.brainres.2006.09.045

How to cite this article: Lin, L., Campbell, J., Oertel, D., & Smith, P. H. (2022). Local targets of T-stellate cells in the ventral cochlear nucleus. *Journal of Comparative Neurology*, *530*, 2820–2834. https://doi.org/10.1002/cne.25378